JOURNAL OF GEOPHYSICAL RESEARCH, VOL. 106, NO. A3, PAGES 3721–3735, MARCH 1, 2001

Collisionless magnetic reconnection: Electron processes and transport modeling

Michael Hesse
Electrodynamics Branch, NASA Goddard Space Flight Center, Greenbelt, Maryland

Joachim Birn
Los Alamos National Laboratory, Los Alamos, New Mexico

Masha Kuznetsova
Raytheon STX, NASA Goddard Space Flight Center, Greenbelt, Maryland

Abstract. Particle-in-cell simulations are used to investigate collisionless magnetic reconnection in thin current sheets, based on the configuration chosen for the Geospace Environment Modeling (GEM) magnetic reconnection challenge [*Birn et al.*, this issue]. The emphasis is on the overall evolution, as well as details of the particle dynamics in the diffusion region. Here electron distributions show clear signatures of nongyrotropy, whereas ion distributions are simpler in structure. The investigations are extended to current sheets of different widths. Here we derive a scaling law for the evolution dependence on current sheet width. Finally, we perform a detailed comparison between a kinetic and Hall-magnetohydrodynamic model of the same system. The comparison shows that although electric fields appear to be quite similar, details of the evolution appear to be considerably different, indicative of the role of further anisotropies in the ion pressures.

1. Introduction

Magnetic reconnection is arguably the most important plasma transport and energy conversion process in space physical plasmas. Magnetic reconnection is involved in the formation and ejection of coronal mass ejecta [e.g., *Gosling et al.*, 1995; *Antiochos et al.*, 2001] and plays a role in coronal heating [e.g., *Priest*, 1984; *Cargill and Klimchuk*, 1997] and facilitates the entry of solar wind plasma and electromagnetic energy into the magnetosphere [*Paschmann et al.*, 1979; *Sonnerup et al.*, 1981]. In the magnetosphere proper, magnetic reconnection converts energy stored in the magnetotail lobes to plasma internal and kinetic energy [e.g., *Nagai et al.*, 1998]. It is also believed to play a role in the formation of the auroral acceleration region [*Atkinson*, 1978; *Haerendel*, 1987]. Therefore magnetic reconnection constitutes a fundamental and ubiquitous element of the Sun-Earth connected system.

Magnetic reconnection relies on the presence of a diffusion region, where collisionless or collisional plasma processes facilitate changes in magnetic connection through the generation of dissipative electric fields. This diffusion region is very localized, extending at most to typical ion Larmor radii. Typical indirect reconnection signatures (contrasted with direct observations of the diffusion region) include the presence of fast flows and plasma heating associated with magnetic field signatures, indicative of the establishment of new magnetic connections. Such indirect signatures are observed remotely in the solar corona [*Brueckner*, 1996], in the solar wind by the magnetic topology of coronal mass ejections (CMEs) [*Gosling et al.*, 1995], and by direct spacecraft observations at the magnetopause and in the magnetotail of the Earth. With the exception of one recent event (J. Scudder, private communication, 1999) the properties of the diffusion region have not been clearly identified in spacecraft observations. This lack of direct observations is due to two effects. First, the localization of the diffusion region and of the processes acting therein requires fast plasma instrumentation, which was not available in the past. Second, and more importantly, the physics of the dissipation region remained a mystery until very recently. Therefore, with little theoretical knowledge of what data signatures are to be expected on such an encounter, it is perhaps not surprising that the search for the diffusion region remains today.

Copyright 2001 by the American Geophysical Union.

Paper number 1999JA001002.
0148-0227/01/1999JA001002$09.00

Recent theoretical and modeling efforts, however, have made great strides toward understanding and more comprehensively describing the inner workings of magnetic reconnection in collisionless plasmas, such as those which dominate in the space regions accessible to direct measurements [*Vasyliunas*, 1975]. Beyond results pertaining to larger scales [e.g., *Krauss-Varban and Omidi*, 1995; *Lin and Swift*, 1996; *Lottermoser et al.*, 1998], we now know that electron physical processes relying on the inertia of individual electrons, expressed as either pressure tensor or bulk inertia effects, are required to facilitate the evolution of the large-scale system. Previous analyses of time-dependent magnetic reconnection [*Hewett et al.*, 1988; *Pritchett*, 1994; *Tanaka*, 1995a, 1995b; *Hesse et al.*, 1998; *Kuznetsova et al.*, 1998; *Hesse and Winske*, 1998; *Shay et al.*, 1998; *Shay and Drake*, 1998; *Horiuchi and Sato*, 1994, 1997; *Cai and Lee*, 1997; *Hesse et al.*, 1999; *Pritchett*, this issue] have therefore begun to shed light on the electron behavior in different parameter regimes, primarily in the regions of low magnetic field. Here it was found that for current sheets of ion inertial length thickness, deviations from gyrotropy in the electron distribution function can give rise to reconnection electric fields via nongyrotropic electron pressures:

$$E_y = -\frac{1}{n_e e}\left(\frac{\partial P_{xye}}{\partial x} + \frac{\partial P_{yze}}{\partial z}\right).$$

Here the y coordinate is aligned with the main current direction, and x and z are perpendicular. This process can be understood as an inertial effect of thermal electrons which bounce in the field reversal region. For current sheets of reduced thicknesses, down to the collisionless skin depth c/ω_e, bulk electron inertial effects might become important and might generate very fast reconnection rates, albeit for very short times.

The purpose of the present study is twofold: First, it studies in detail the evolution properties of a fully electrodynamic, particle-in-cell simulation of magnetic reconnection. Here we focus on the mechanisms determining the reconnection rate, the electron outflow velocity from the reconnection region, and the structure of ion and electron distribution functions in the reconnection region proper and adjacent to it. This is followed by investigations of the impact of the initial sheet thickness and electron mass. We will derive a simple argument explaining the effect of the plasma sheet thickness on the overall evolution.

Second, this study contributes to a model comparison a fully kinetic simulation of a given system. The parameters of the system under investigation are those of the "reconnection challenge," defined by a modeling working group within the Geospace Environment Modeling (GEM) program of the National Science Foundation. The goal of this initiative is to compare simulations of the same reconnection configurations aiming at understanding the physics underlying the reconnection process, as well as deriving ways to represent microphysical processes in macroscopic plasma models. As a further contribution to this quest, we also include a fluid, Hall-MHD model of the same system. Similar Hall-MHD efforts have been undertaken by *Ma and Bhattacharjee* [1996] and as part of the GEM challenge by *Otto* [this issue], *Shay et al*. [this issue], and *Birn and Hesse* [this issue]. This last part of the study includes a detailed comparison between the kinetic and Hall-MHD models.

2. Numerical Approach and Initial Conditions

For the purpose of the present investigation we use a two-and-a-half-dimensional version of our fully electromagnetic particle-in-cell code. The scheme is based on the Buneman layout of currents and fields on a rectangular grid [e.g., *Villasenor and Buneman*, 1992]. Particles are advanced by a second-order, implicit leapfrog algorithm. Densities and fluxes are accumulated on the grid, using a rectangular particle shape function. Charge conservation is guaranteed by the iterative application of a Langdon-Marder-type [*Langdon*, 1992] correction to the electric field. The electromagnetic fields are integrated implicitly to avoid the Courant constraint on the propagation of light waves. The light wave damping in the implicit scheme also allows us to use simple reflecting boundary conditions for the electromagnetic fields at the z boundaries (periodicity is assumed in x). Comparisons between runs performed with the explicit and implicit algorithms showed excellent agreement.

Ions are assumed to be protons in the following investigations. Further, we normalize lengths to the ion inertial lengths $c/\omega_i = c(e^2 n_0/\varepsilon_0 m_i)^{-1/2}$ using a current sheet density n_0, and times are normalized to the inverse of the ion cyclotron frequency $\Omega_i = eB_0/m_i$ in the asymptotic magnetic field B_0 unless noted otherwise. The magnetic field is normalized to the asymptotic value B_0 for large z. Velocities are normalized to the Alfvén speed $v_A = B_0/\sqrt{\mu_o m_p n_0}$. Consequently, current densities and electric fields are normalized to $j_0 = B_0/(\mu_0 c/\omega_i)$ and $E_0 = v_A B_0$, respectively, and the resistivity is measured in units of $\eta_0 = \mu_0 v_A c/\omega_i$. The system dimensions and initial conditions follow the GEM magnetic reconnection challenge [*Birn et al*., this issue]. In the present calculations the system dimensions are $L_z = 12.8c/\omega_i$ and $L_x = 25.6c/\omega_i$ with 400×200 cells in x and z directions, respectively. A time step of an inverse electron plasma frequency $\omega_e \Delta t = 1$ is used. The ratio ω_e/Ω_e is set to a numerical value of 5.

The focus of the research presented here is on the mechanisms of collisionless dissipation supporting the magnetic reconnection process rather than on the question of how magnetic reconnection starts. Thus we set up the simulations with an X-type neutral point of the poloidal magnetic field. Accordingly, the initial equilibrium configuration was chosen as a Harris sheet equilibrium in the x-z plane, with the initial current density y-aligned,

$$B_x = \tanh\,(z/\lambda),$$

with an additional perturbation of the form

$$B_{xp} = \frac{a_0\pi}{L_z}\cos\,(2\pi x/L_x)\,\sin\,(\pi z/L_z),$$

$$B_{zp} = -\frac{2a_0\pi}{L_x}\sin\,(2\pi x/L_x)\,\cos\,(\pi z/L_z),$$

and a "guide field" of

$$B_y = B_{y0}.$$

Here the perturbation amplitude $a_0 = 0.1$ results in a B_z amplitude of ~2.5% of the asymptotic magnetic field strength. The sheet half-thickness, in terms of ion scale lengths, is adopted to be $\lambda = 0.5$ for the main investigation but is varied later.

Four particle species, two of ions and electrons each, were integrated in each run. The first set of ion and electron species establishes the pressure and currents. The second set of species constitutes a constant density level background $n_b = 0.2$. Background temperatures are identical to the temperatures of the current-carrying species $T_i + T_e = 0.5$. The particle simulations used 4×10^6 ions and electrons each for the foreground and 2×10^6 ions and electrons each for the background.

Periodic boundary conditions were employed at $x = 0$ and $x = 25.6$. At the top and bottom boundaries, particles are specularly reflected. The electron-ion temperature ratio in all runs is chosen as $T_e/T_i = 0.2$. The mass ratio, the essential parameter in the present investigation, is set to $m_i/m_e = 25$.

3. Results

Plate 1 displays the magnetic field evolution, together with the total current density (color-coded). The evolution starts rapidly from the initial perturbation, after the current density has rearranged itself in the dissipation region. A common feature of the evolution, also found in kinetic simulations with different mass ratios [*Hesse et al.*, 1999], Hall-MHD modeling, and MHD modeling of the system under investigation, is the bifurcation of the initial reconnection site. Splitting the single reconnection site into two creates a magnetic island, which persists until after $\Omega_i t = 15$ in the present simulation. At later times, the island gets dissipated as one of the two new reconnection sites becomes dominant ($\Omega_i t = 20$).

Plate 1 also shows the common behavior of the current density in the vicinity of an active X point: While the central diffusion region features reduced current density concentrated in a thin current sheet, the adjacent region, where the normal magnetic field appears enhanced, features a strongly enhanced current density. Similar properties have been found in earlier hybrid [*Kuznetsova et al.*, 1998, this issue] and electromagnetic simulations [*Hesse and Winske*, 1998; *Hesse et al.*, 1999].

Figure 1 displays the individual ion and electron contributions to the y component of the current density in the vicinity of the reconnection region for $\Omega_i t = 15$ along the $z = 0$ axis. Figure 1 shows that the ion contribution to the current in the diffusion region is considerably smaller than the one of the electrons. The electrons are the dominant current carriers and appear to be concentrated in a current sheet of about an electron skin depth thickness in the z direction; see Plate 1. This thickness can also be estimated by the electron bounce amplitude in a magnetic field reversal [*Hesse et al.*, 1999].

It has been noted for some time that magnetic reconnection can be strongly accelerated in current sheets thin enough to render Hall effects important [*Drake and Mandt*, 1994; *Hesse and Winske*, 1994]. In these situations, magnetic flux is convected by the electron flow velocity $\mathbf{v}_e$,

$$\frac{\partial \mathbf{B}}{\partial t} \approx \nabla \times (\mathbf{v}_e \times \mathbf{B}), \tag{1}$$

instead of the ion velocity as in MHD. The electron flow velocity can be expressed by the total current density $\mathbf{j}$, the ion and electron densities n_i and n_e, and the ion flow velocity $\mathbf{v}_i$,

$$\mathbf{v}_e = n_e^{-1}(n_i \mathbf{v}_i - \mathbf{j}), \tag{2}$$

which, to a very good approximation, reduces to

$$\mathbf{v}_e = \mathbf{v}_i - n^{-1}\mathbf{j}, \tag{3}$$

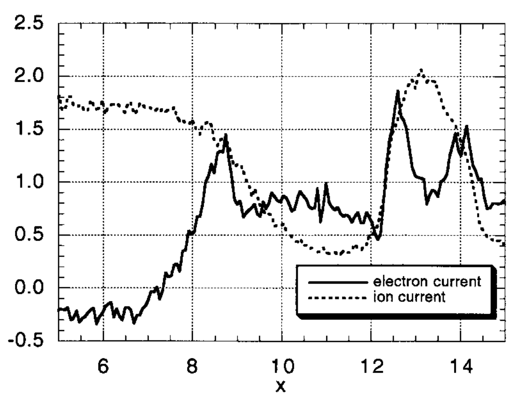

Figure 1. Ion and electron current densities in the vicinity of the X point for $\Omega_i t = 15$. Figure 1 shows that most of the current in the reconnection region is provided by the electrons.

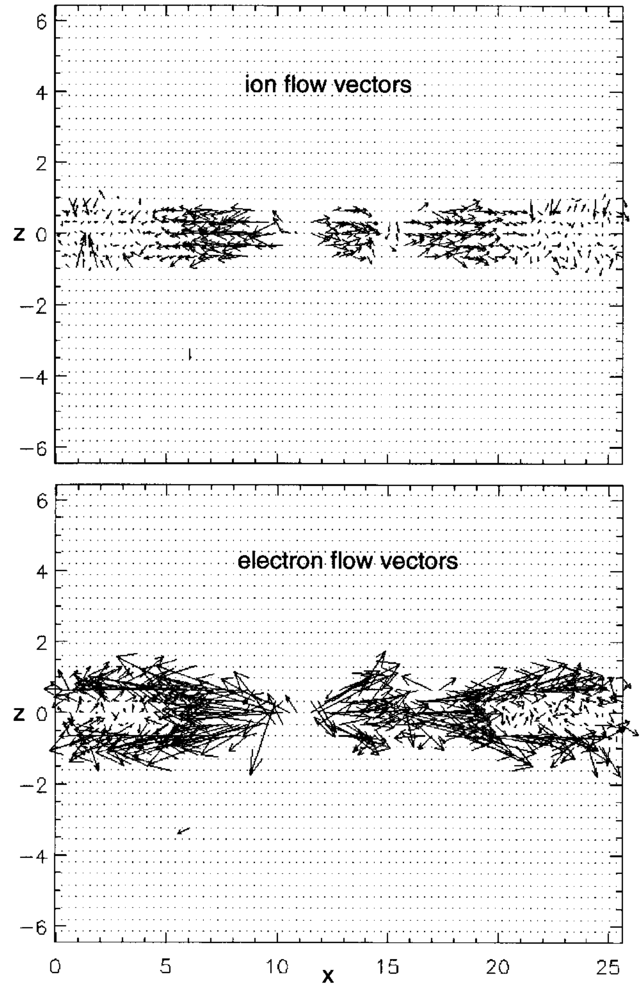

Figure 2. Ion and electron flow vectors for $\Omega_i t = 15$. Vectors for regions with density $n < 0.1$ are omitted to reduce noise.

assuming singly charged ions with $n = n_i = n_e$. Equation (3) demonstrates the importance of the current density in the x and z directions in the reconnection process.

Figure 2, which displays ion and electron flow vectors for $t = 15$, shows a very large difference between the flow speeds in the neighborhood of the dissipation region proper. While ion velocities remain well below the Alfvén speed, electron flows are considerably faster, ranging up to $v_{e,\max} \approx 2v_A$ [see also, e.g., *Hesse et al.*, 1999].

The difference between these flow speeds is, by virtue of (3), given by the current density in the x-z plane $\mathbf{j}_p$. In the present translationally invariant model, this current density derives from a gradient of the magnetic field in the invariant direction B_y,

$$\mathbf{j}_p = \nabla B_y \times \mathbf{e}_y. \tag{4}$$

The quadrupolar structure of B_y, shown in Plate 2, again for $t = 15$, provides the gradients which support the current flow in (4). It should be noted that the current flow is opposite to the particle flow, i.e., into the reconnection region in the horizontal direction, and out of it vertically. Similar quadrupolar magnetic fields have been seen earlier in hybrid simulations of

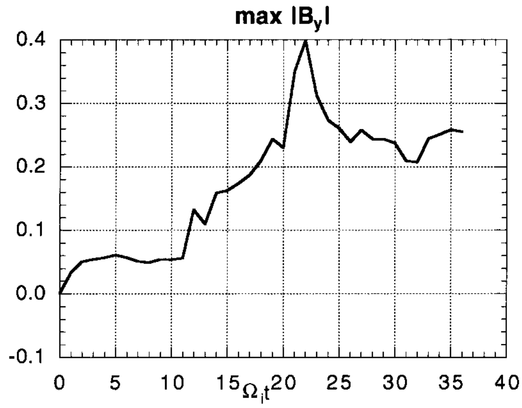

Figure 3. Time evolution of the peak value of the out-of-plane magnetic field component B_y.

magnetic reconnection [*Drake and Mandt*, 1994; *Hesse and Winske*, 1994].

Figure 3 displays the peak amplitude of B_y as a function of time during the entire simulation. The peak amplitude of B_y can be comparable to the asymptotic lobe magnetic field, i.e., assume a magnitude of 0.4, during the later part of the evolution. The reduction of B_y at the very latest times is associated with an overall reduction of the rate of magnetic reconnection due to a lack of magnetic energy in the lobes, and the compressive effects of magnetic flux and plasma in the large island region.

The reconnection rate, or, equivalently, the reconnection electric field, is displayed in Figure 4. During the phase of dual reconnection sites the electric field at the most advanced X point is shown. Figure 4 displays an initial lag of some eight ion cyclotron times. This time interval appears to be needed to set up the proper conditions in the reconnection region. After $t = 10$ the reconnection electric field increases strongly to peak values of, in units of $v_A B_0$, $E_{\max} \approx 0.3$. The above mentioned effects of finite system size lead to a subsequent reduction in reconnection rate. We point out that the presence of a background population prevents the reconnection process from converting into an electromagnetic wave as reconnection reaches the lobes, as found in simulations of a pure Harris equilibrium [*Hesse and Winske*, 1998].

The peak ion and electron flow velocities in the x direction are plotted in Figure 5 versus the instantaneous value of the reconnection electric field. Here we find the aforementioned difference between peak velocities. Beyond these differences, it is noteworthy that both electron and ion flow velocities exhibit a pronounced correlation with the reconnection electric field. While this is to be expected for the electrons by virtue of (1), this relation is less obvious for the ion flow. Figure 5 shows, however, that the reconnection electric field appears to indirectly also regulate the ion flow behavior. Therefore some features of the single-fluid behavior, where ions and electron move in unison, are found also in a kinetic model, albeit with a much weaker coupling between the particle species.

4. Distribution Functions in the Dissipation Region

Recent investigations of the magnetic reconnection process based on hybrid and fully electromagnetic calculations have shown that the dissipation process underlying magnetic reconnection is, to the largest part, supported by gradients of the electron pressure tensor in the equation

$$\mathbf{E} + \mathbf{v}_e \times \mathbf{B} = -\frac{1}{n_e e} \nabla \cdot \underline{\mathbf{P}}_e + \frac{m_e}{e}\left(\frac{\partial \mathbf{v}_e}{\partial t} + \mathbf{v}_e \cdot \nabla \mathbf{v}_e\right). \qquad (5)$$

Here $\mathbf{v}_e$, n_e, $-e$, m_e, and $\underline{\mathbf{P}}_e$ denote velocity, number density, charge, mass, and pressure tensor of the electrons, respectively [*Hesse and Winske*, 1993, 1998; *Kuznetsova et al.*, 1998; *Hesse et al.*, 1999]. *Hesse et al.* [1999] argued that the structure of the dissipation region is determined by the typical dimension of the meandering electron orbits in magnetic field reversals, thereby quantifying an argument of *Horiuchi and Sato* [1994, 1997]. Besides showing quantitative agreement between the scale sizes expected from orbit analysis and those found in the actual simulation, no direct analysis of the structure of the electron distribution function was performed by *Hesse et al.* [1999].

Plate 3a displays the electron distribution function, combining foreground and background populations directly at, or just adjacent to, the major dissipation region for $\Omega_i t = 15$. For the top panel, representing the location around the maximum of the off-diagonal pressure tensor component P_{xye}, particles were accumulated in the interval $10 \leq x \leq 11$ and $-0.5 \leq z \leq 0.5$. A total of 17,400 electron particles was used for the

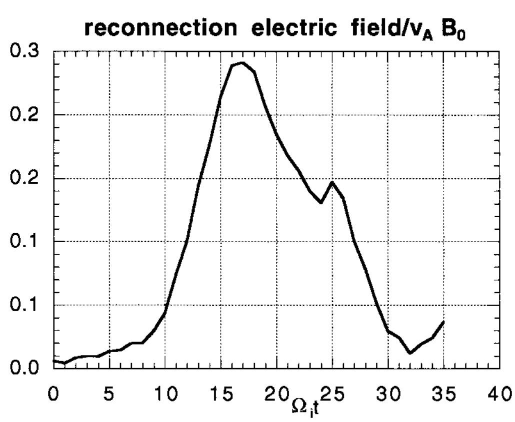

Figure 4. Electric field at the active X point in the kinetic model.

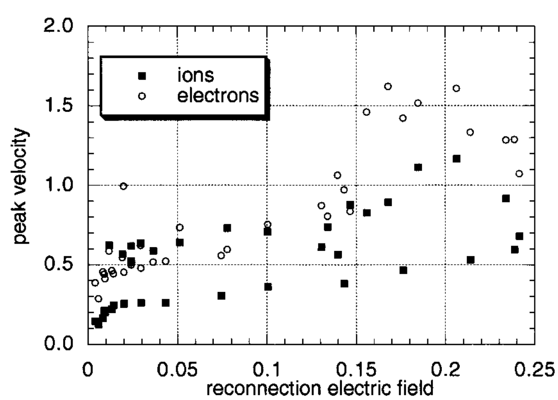

Figure 5. Maximum ion and electron flow velocity x components versus instantaneous value of the reconnection electric field.

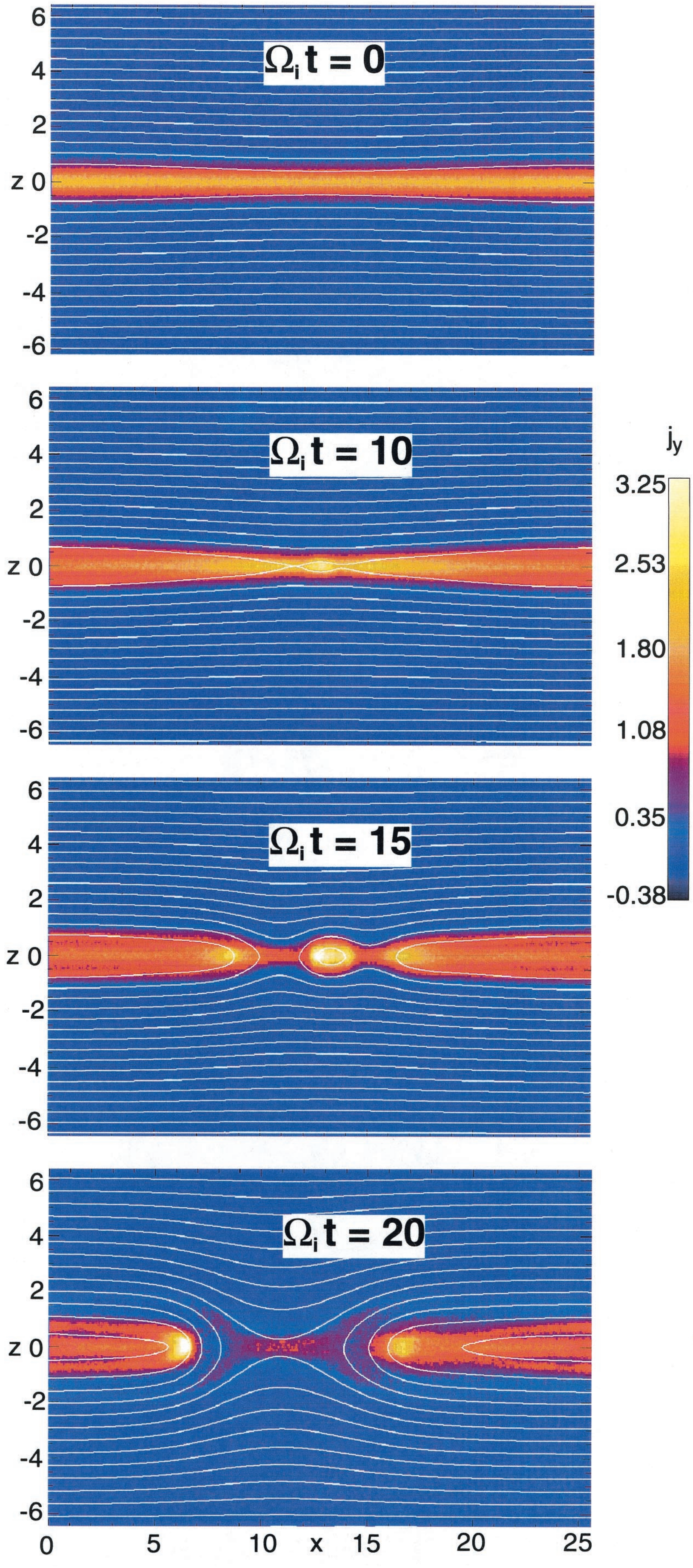

Plate 1. Magnetic field evolution and current density (color-coded) evolution for the standard run. Plate 1 shows strong changes brought about by magnetic reconnection, initiated by the initial perturbation.

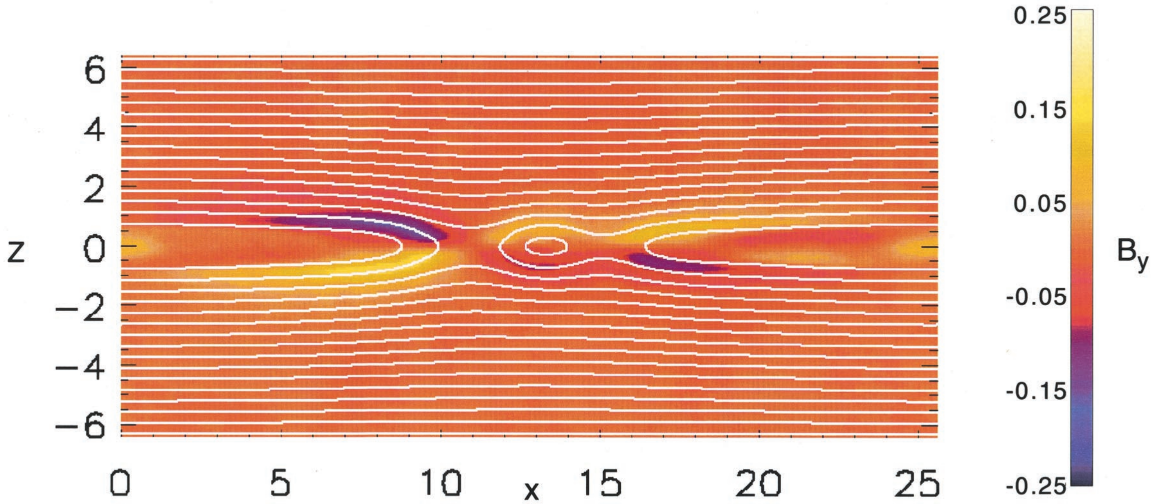

Plate 2. Out-of-plane magnetic field component B_y for $\Omega_i t = 15$.

construction of the distribution function. Velocity units are those of the Alfvén speed. Plate 3a shows a very nonsymmetric and nongyrotropic electron distribution with a significant velocity offset in the negative y direction, matching the strong electron current density in that region. This velocity is the signature of some acceleration of the bulk electron fluid, which is, however, insufficient to support the total reconnection electric field [*Hesse and Winske*, 1998]. The asymmetry in the u_x direction indicates electron bulk flow in the negative x direction, away from the dissipation region.

The nongyrotropic nature of the electron distribution corresponds to a positive value of the pressure tensor component P_{xye}. Electron particles accelerated by the reconnection electric field experience the Lorentz force of the negative B_z enhancement at the left side of the dissipation region, accelerating or turning the particle into the negative x direction. The directional change should be most pronounced for electrons with significant u_y velocity components, leading to a larger shear effect for electrons with larger u_y. This argument explains the structure of the top distribution in Plate 3a, where most of the bulk flow in the negative x direction appears to be due to particles with large negative u_y velocity components. Clearly, such behavior is possible only if the electrons are only partially magnetized; otherwise, a finite bulk flow perpendicular to the magnetic field would have to be supported by the cold bulk of the distribution.

The electron distribution in a region centered around the X point proper is displayed in the bottom panel of Plate 3a. Particles were accumulated in the interval $10 \leq x \leq 11$ and $-0.5 \leq z \leq 0.5$. A total of 15,400 electron particles was used for the construction of the distribution function. The distribution consists of a warm electron core distribution, with an extended tail in the negative u_y direction, which is symmetric in u_x. Some effects of the adjacent normal magnetic field B_z can be discerned at the higher negative values of u_y. These effects are unavoidable if a sufficiently large number of particles were to be used for distribution function generation. Nevertheless, the bottom panel features a quite strong electron current in the negative y direction, which is not supported by the bulk of the distribution. Again, this latter feature is a result of the lack of electron magnetization in the diffusion region.

While the electrons are strongly affected by the increases of the normal magnetic field B_z in the vicinity of the X point, the ions show much less of a turnaround by the ambient normal magnetic field. This is evident from the distributions shown in Plate 3b. Ion distributions were accumulated in the same intervals as for the electrons. Values of 27,000 and 23,400 ion particles were integrated for the top and bottom panels, respectively. The difference in particle numbers between ions and electrons does not imply a large charge density. Instead, the electron particles involve a larger contribution of the background population, with a larger charge per macroparticle.

Both panels of Plate 3b show strong anisotropy but much less asymmetry than the electron distribution taken directly at the X point, with reversed velocities in the y direction, and generally much smaller velocities, leading to smaller current density contributions and smaller bulk flow in the x direction. Both panels show a pronounced tail in the positive u_y direction, presumably due to ion acceleration by both the reconnection electric field and the Hall electric field generated by the electron flow in the immediate vicinity. In the latter region, ions are still unmagnetized and thereby susceptible to acceleration by electric fields generated by the motion of magnetized electrons. A small effect of the normal magnetic field, primarily on the fastest ions, can be discerned in the top panel of Plate 3b. Ions moving rapidly in the current direction feature a small velocity component in the negative u_x direction, corresponding to slow outflow from the dissipation region.

5. Sheet Thickness and Electron Mass Effects

The above investigations were based on a particle-in-cell simulation of a specific system with a given current sheet width and a given electron-ion mass ratio. While there are many more parameters which could and should be varied to study their effect on the overall evolution, we here concentrate on the effects of sheet width. Previous results [*Hesse et al.*, 1999] pertaining to electron mass effects will also be summarized below, for the purpose of an introduction to section 6.

To investigate the effects of the current sheet width, we performed two additional simulations, with a total sheet thickness of $0.5c/\omega_i$ and $2c/\omega_i$, respectively. All other parameters are identical to the original run, including the form of the

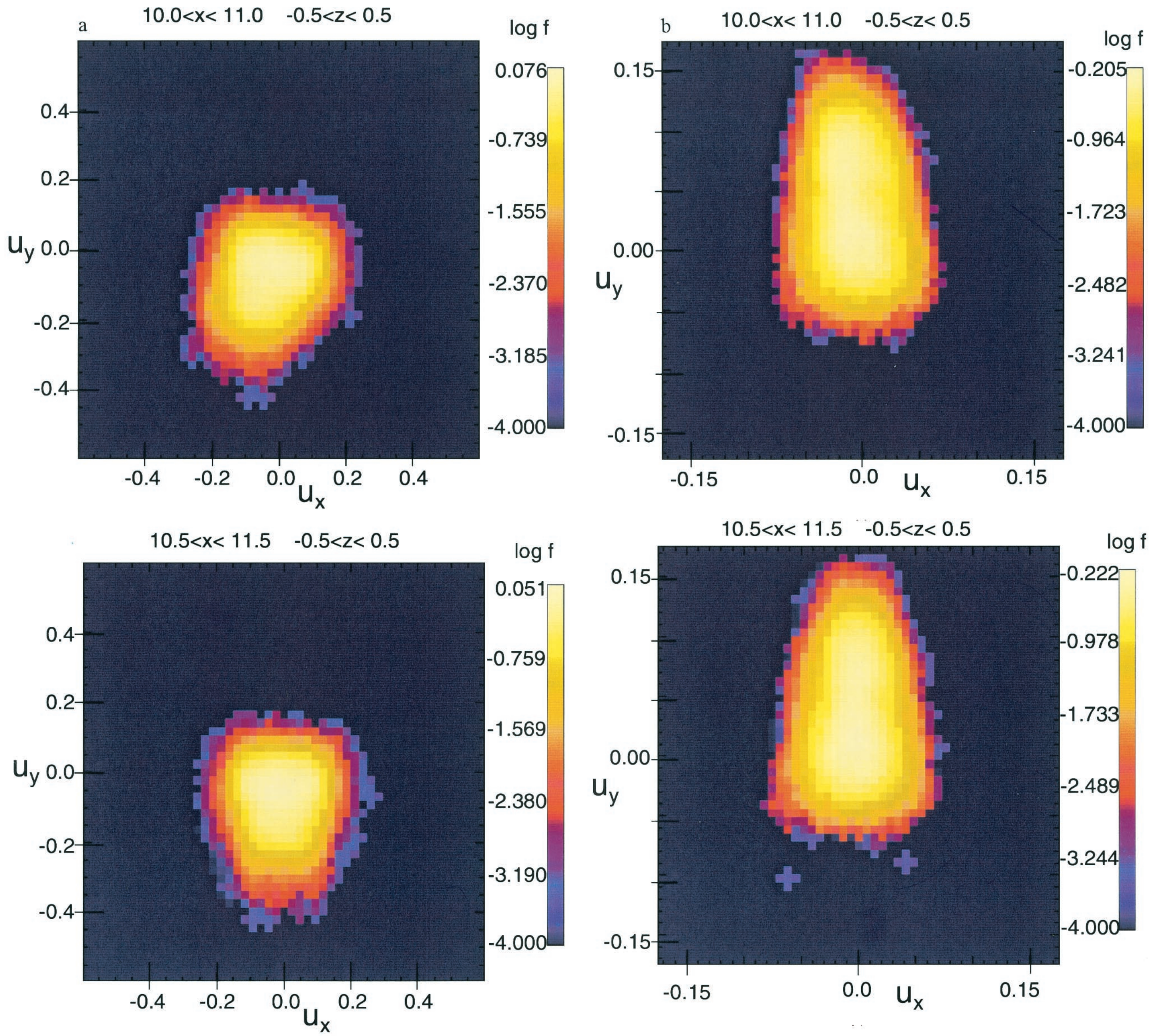

Plate 3. (a) Electron distributions for $\Omega_i t = 15$, (top) adjacent to the major X point and (bottom) right at the X point. The color coding corresponds to the logarithm of the phase space density. (b) Ion distributions for $\Omega_i t = 15$ (top) adjacent to the major X point and (bottom) right at the X point.

initial perturbation. The evolution of magnetic fields and current densities for these two runs is shown in Plates 4a and 4b, in the same format as Plate 1. The rapid evolution of the very thin sheet, shown in Plate 4a, features the formation of multiple islands (seen at $t = 6$). The majority of these small islands dissipate rapidly such that only one remains in the bottom panel. This latter island disappears as well during the subsequent evolution.

The thicker sheet undergoes a much slower reconnection process. Plate 4b also shows a much simpler X point structure, consisting of a single X point located at the center of the initial perturbation and persisting during the entire evolution. The typical current density enhancements in the neighborhood of the reconnection site are present but strongly reduced in amplitude, consistent with the slower evolution in comparison to the other two runs.

Figure 6 shows the time evolutions of the normal magnetic flux, again integrated from the major X point to the major O point, for all three runs. Figure 6 quantifies the impressions obtained from Plates 1, 4a, and 4b, showing faster evolutions for smaller sheet thicknesses. A simple way to understand this might be obtained from the following analysis: The total force per unit length in the y direction acting, in the x direction, on the plasma is given by

$$F = \int dx\, dz\, B_z j_y, \tag{6}$$

where the integral extends over the current sheet width in z and one half axis in x. The mass per unit length in y accelerated by this force is given by

$$M = (m_i + m_e) \int dx\, dz\, n, \tag{7}$$

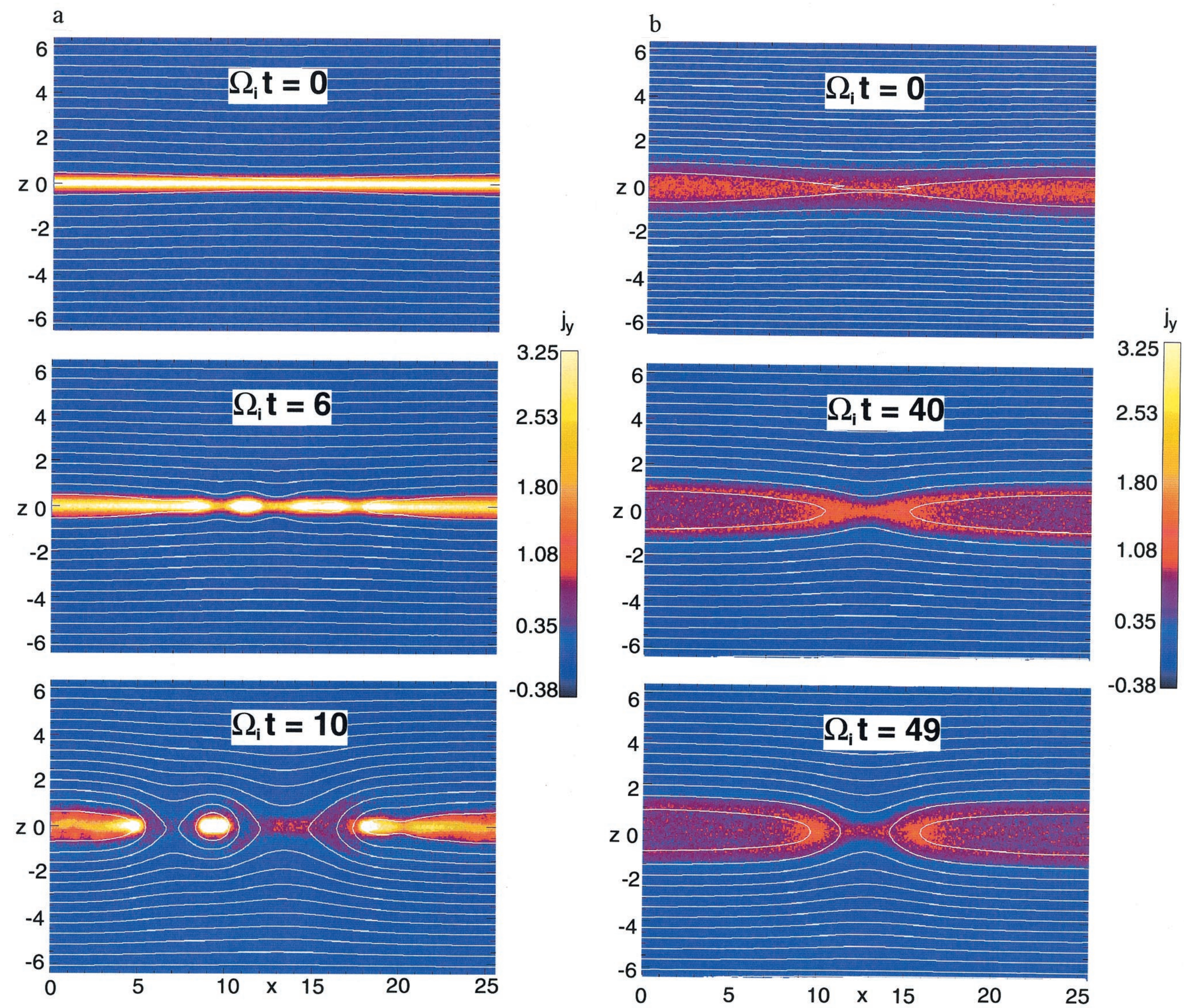

Plate 4. (a) Magnetic field evolution and current density (color-coded) evolution for the thin sheet run. (b) Magnetic field evolution and current density (color-coded) evolution for the thick sheet run.

where again the integral extends over the plasma sheet width and one half-axis. Replacing integrands with typical values, one finds an equation for the acceleration A,

$$(m_i + m_e) L_x L_z n_t A \approx L_x L_z j_{yt} B_{zt}, \tag{8}$$

with n_t, j_{yt}, and B_{zt} denoting typical values of density, current density, and normal magnetic field, respectively. L_x represents the half-length of the x axis, and L_z represents the plasma sheet width. Clearly, the latter two parameters drop out, and B_{zt} is initially independent on the sheet width. On the other hand, j_{yt} is proportional to the inverse sheet width, and we assume n_t to be independent to first approximation on the sheet width. It then follows immediately that the acceleration

$$A \sim L_z^{-1}, \tag{9}$$

implying a similar inverse-linear dependence for velocity and, consequentially, electric fields.

The validity of this simple linear analysis can be checked in two ways. For the first, Figure 7 displays the dependence of the maximum value of the reconnection electric field on inverse sheet thickness. The graph features an almost perfect linear behavior, indicating the validity of the above argument. A further, more detailed analysis can be obtained by comparing the evolution times from the initial state to given values of the total reconnected magnetic flux. On the basis of the above arguments, one would expect a linear dependence of the evolution time on the sheet width. The results of this study are shown in Figure 8, for three different levels of reconnected magnetic flux. In contrast to the maximum growth rate, expressed by the maximum reconnection electric field, the evolution time clearly shows nonlinear effects; it increases more strongly for thicker sheets. The differences are possibly related to the fact that the evolution time is an integrated quantity, whereas the maximum reconnection rate is an instantaneous property, such as our simple estimate.

Two other parameters might be crucial in determining the overall evolution, the electron mass and a magnetic field component in the invariant direction. *Hesse et al.* [1999] studied the effects of varying the electron mass in the range from 1/9 to 1/100 of the ion mass, keeping all other physical parameters

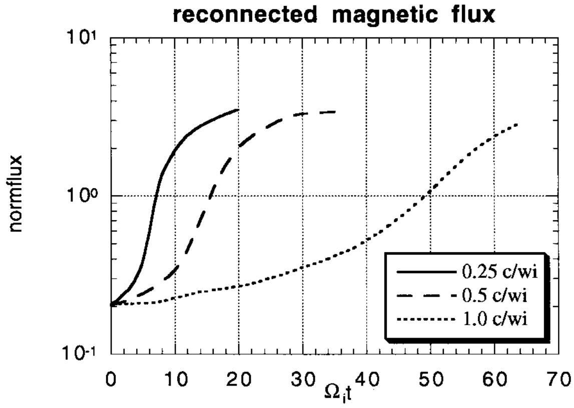

Figure 6. Time evolution of the magnetic flux normal to the current sheet for all three kinetic simulations.

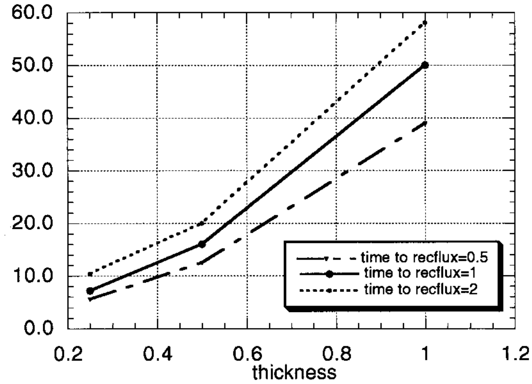

Figure 8. Elapsed simulation times, in units of the inverse ion cyclotron period, until a certain level of magnetic flux normal to the current sheet is reached. Figure 8 shows a clear ordering for all three flux levels considered but some deviation from the predicted linear dependence on current sheet width.

fixed. They also included a model with a $B_y = 0.3$ magnetic field component (in units of the lobe magnetic field), which was estimated to be large enough to magnetize electrons and thereby destroy the nongyrotropy of the electron distribution. The time evolution of the reconnected magnetic flux is shown in Plate 5a for all these cases. Beyond some small differences in the onset timing of the fast evolution, the nonlinear behavior of the reconnected magnetic flux appears to be almost independent of the electron mass. The same appears to be true for the simulation with finite B_y magnetic field component, as long as this "guide field" remains small enough to not contribute significantly to the magnetic pressure in the system.

This result was motivation for *Hesse et al.* [1999] to pursue the idea that reconnection timescales might, in this nonlinear stage, be determined by the large-scale, i.e., ion dominated, dynamics. If this proves to be correct, a much simpler dissipation model, for example, resistivity based, might be sufficient to foster magnetic reconnection if the large-scale dynamics is sufficiently well represented. Using a Hall-MHD model, *Hesse et al.* [1999] showed that similar reconnection rates could indeed be obtained from these Hall-MHD calculations if suitable resistivity models were adopted. In section 6 we will take their analysis a step further by presenting results of a further improved Hall-MHD calculation, together with a detailed comparison between Hall-MHD and electromagnetic calculations.

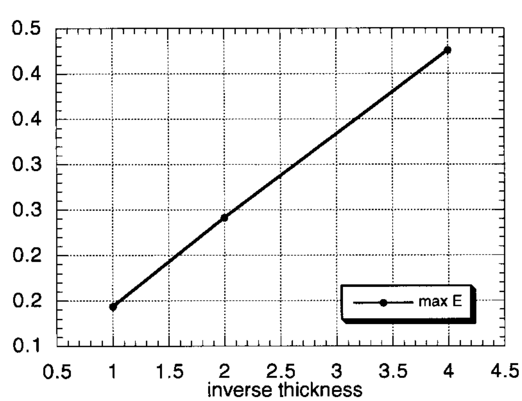

Figure 7. Dependence of the maximum reconnection electric field on the inverse of the initial current sheet width. Figure 7 shows an almost perfect linear behavior.

6. Hall-MHD Simulation

Hall-MHD, as a fluid treatment, constitutes a substantial simplification of the kinetic model discussed in section 5. Within Hall-MHD, no kinetic effects are considered at all, excluding also the effects of anisotropic pressures for both ions and electrons. For simplicity, only ion pressure is considered, where a polytropic pressure law with resistive heating terms is commonly adopted. The electron pressure might have some effects on the details of the (resistive) reconnection region. Since we are not interested in a correct representation of the latter, we here ignore the electron pressure altogether. Dissipation is based on an ad hoc resistivity model, although we will include electron inertia effects to limit the Whistler dispersion. Denoting by ρ the total mass density, by $\mathbf{v}$ the total flow velocity, by p the total pressure, by $\gamma = 5/3$ the polytropic index, and by η the resistivity, the Hall-MHD equations used in our investigation assume the following dimensionless form:
Equation of continuity

$$\frac{\partial \rho}{\partial t} + \nabla \cdot (\rho \mathbf{v}) = 0, \qquad (10)$$

Momentum equation

$$\rho\left(\frac{\partial \mathbf{v}}{\partial t} + \mathbf{v} \cdot \nabla \mathbf{v}\right) = -\nabla p + \mathbf{j} \times \mathbf{B}, \qquad (11)$$

Faraday's law

$$\frac{\partial \mathbf{B}}{\partial t} = -\nabla \times \mathbf{E}, \qquad (12)$$

Ohm's law

$$\mathbf{E} = -\mathbf{v} \times \mathbf{B} + \eta \mathbf{j} + \frac{1}{\rho}\mathbf{j} \times \mathbf{B} + \frac{m_e}{\rho}\frac{\partial \mathbf{j}}{\partial t}, \qquad (13)$$

Energy equation

$$\frac{\partial p}{\partial t} = -\mathbf{v} \cdot \nabla p - \gamma p \nabla \cdot \mathbf{v} + (\gamma - 1)\eta j^2. \qquad (14)$$

Equations (10)–(14) are identical to the standard resistive MHD model, with the exception of the last two terms on the right-hand side of Ohm's law (equation (13)). The addition of

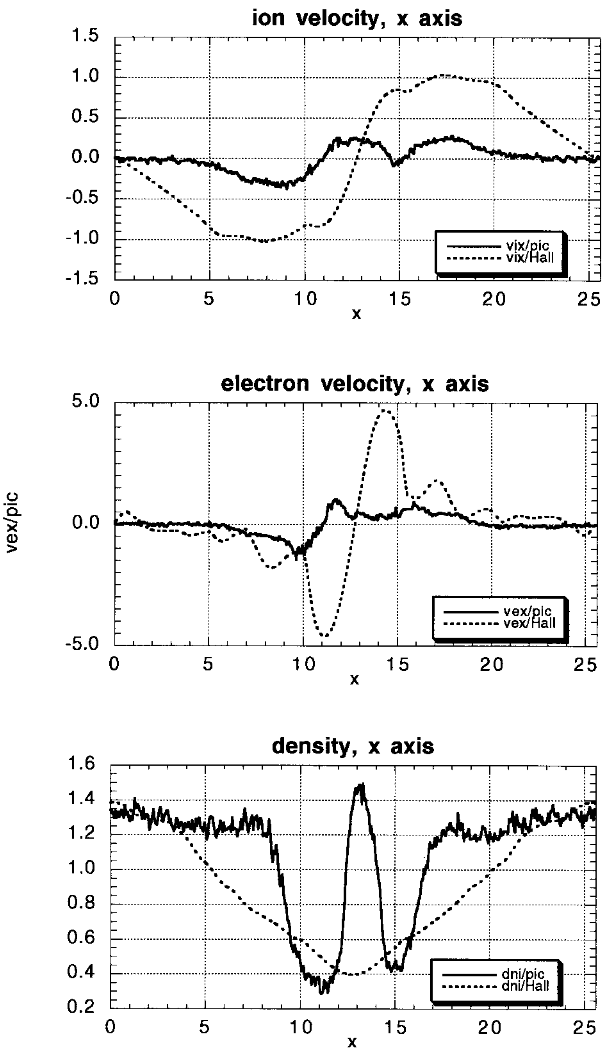

Figure 9. Comparison along the x axis between (top) ion velocities, (middle) electron velocities, and (bottom) densities. Comparisons are for the particle simulation (solid lines) and Hall-MHD simulations (dotted lines), all for $\Omega_i t = 15$. In particular, the velocities show large differences, with much higher flows in the Hall-MHD model.

the Hall term $\mathbf{j} \times \mathbf{B}$ changes the wave characteristics by adding Whistler modes to the spectrum of the equations. The last term on the right-hand side, a reduced form of the complete electron inertia term, is included here in order to stabilize the calculations by adding a cutoff to the Whistler modes at the electron cyclotron frequency. For the purpose of the present investigations we choose an electron mass of $m_e = 1/100$. A simple analysis [*Hesse et al.*, 1999] shows that this term is insufficient to provide the dissipation required for the reconnection process.

Equations (10)–(14) are integrated by a standard leapfrog technique which includes a flux-limiting routine and an elliptical solver for the electron inertial effects. The initial conditions for the ion fluid and the electromagnetic fields are identical to the ones described for the kinetic models in section 2, with the sole exception being that the initial current density is entirely provided by ion flow in the y direction. A grid of 200×100 cells is used for the calculations.

On the basis of the above results, we assume that the exact form of the dissipation employed in Ohm's law might be irrelevant, as long as it is sufficiently large and supports $\mathbf{E} \cdot \mathbf{j} > 0$ in the diffusion region. In our case this implies the need to select a sufficiently large resistivity η such that at the neutral point a significant electric field magnitude $E = \eta j$ can be reached by the system without an excessively large current density. Furthermore, a localization of the resistivity is desirable in order to avoid strong diffusion outside the reconnection region proper. Lack of localization has been shown to strongly slow down the evolution [*Hesse et al.*, 1999]. With this in mind, we design our resistive model as follows:

$$\eta(x, z) = \eta_0[1 + \eta_1 \cosh^{-1}(r)] \qquad j > 2, \qquad (15a)$$

with $r = \sqrt{(x - x_r)^2/2 + z^2)}$ and x_r denoting the x coordinate of the major X point, or

$$\eta = \eta_0 \qquad j \leq 2. \qquad (15b)$$

The constant $\eta_0 = 10^{-4}$ corresponds to an overall Lundquist number of $S = 5 \times 10^3$, and $\eta_1 = 50$ was chosen for the amplitude of the localized resistivity enhancement.

Plate 6 displays, in the same format as Plate 1, the time evolution of the magnetic field and current density in this Hall-MHD run. Flow vectors are shown also. Plate 6 shows some striking similarities with Plate 1. Differences are found in the absence of magnetic islands in the Hall-MHD run and a more pronounced symmetry about the center in the x direction, despite the movable location of the reconnection site.

The time evolution of the reconnected magnetic flux is shown in Plate 5b, together with the kinetic result from above. Also shown are the results for different values of η_1, ranging from $\eta_1 = 100$ to $\eta_1 = 5$. Despite the evident differences in the apparent evolutions (see Plates 1 and 6), the time evolution of the reconnected flux appears to be very similar, indicative of similar magnitudes of the reconnection electric field. We point out that the cessation of the Hall-MHD evolution curves is due to a lack of code convergence, generated by an extremely low density. This is a typical limitation of physical approaches which do not solve the full set of Maxwell's equations (i.e., including the displacement current).

We also remark that changes of the resistivity value in the Hall-MHD run do not generate different growth rates, as long as the resistivity remains localized. The only difference between Hall-MHD runs with different resistivity amplitudes is found in the time of onset of the fast evolution. We explain this difference by the time it takes to form in the reconnection region a current sheet thin enough to provide sufficient dissipation.

The similarity between kinetic and Hall-MHD results, however, is deceptive, as can be inferred from a detailed comparison between the simulation results at a given time. For this purpose we select a time of $\Omega_i t = 15$, where the level of normal magnetic flux has roughly reached the dimensionless value of 1. At this time we now compare the variations of characteristic quantities along the x axis of the simulation domain. The top panel of Figure 9 displays the ion flow velocities for both simulations. It is obvious from the graphs that the Hall model generates much higher flow speeds than the kinetic model does. The same appears to be true for the electron flow speeds, shown in the middle panel. Here the pattern of the Hall model resembles kinetic simulations for smaller electron masses, which feature more localized electron flows of high velocities [*Hesse et al.*, 1999]. The densities, shown in the bot-

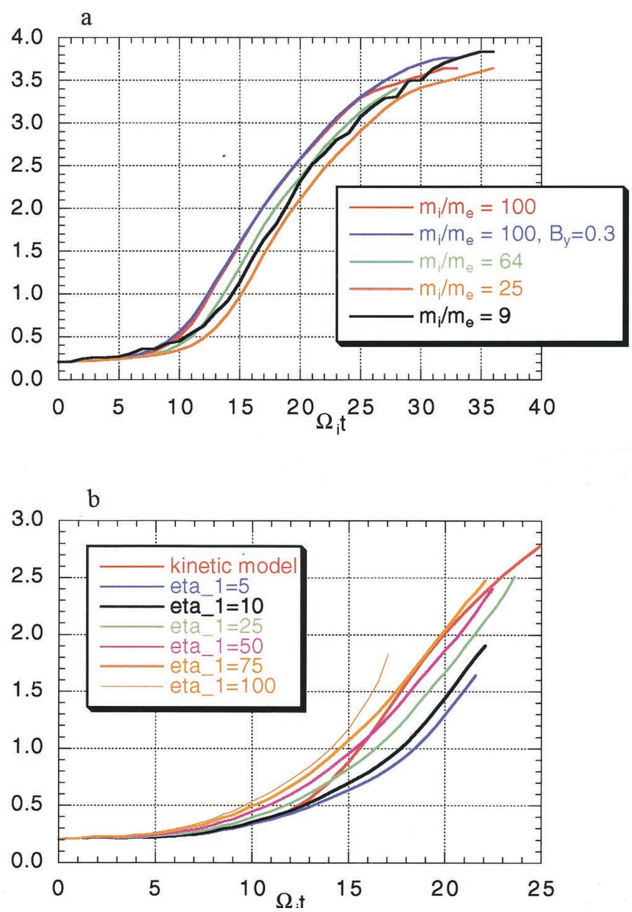

Plate 5. (a) Time evolution of the magnetic flux normal to the current sheet for a set of kinetic simulations with different electron masses and, in one case, a guide magnetic field (B_y = 0.3). All simulations feature essentially the same nonlinear behavior, as manifested in the apparent near identity of the individual curves. (b) Time evolution of the magnetic flux normal to the current sheet for the kinetic simulation, and the Hall-MHD model for different peak values of the resistivity η_1. Despite the difference in dissipation models and resistivity amplitude, the growth rates are very similar. The difference in onset times of the fast evolution can be attributed to the development time for a sufficiently thin current sheet in the individual model.

tom panel, appear similar (besides the island structure still present in the kinetic model) with a broader density cutout in the Hall-MHD case. This latter is likely due to the larger size of the dissipation region in the Hall-MHD model.

The comparison continues with Figure 10, the top panel of which depicts the current density in the invariant direction for both runs. While, at first glance, the amplitudes appear to be similar, a remarkable difference exists in that the current density peaks are adjacent to the X point in the kinetic model, whereas the maximum is right at the X point in the Hall-MHD model. The latter, however, is not very surprising in light of the fact that the dissipative electric field in this case given by $E_d = \eta \mathbf{j}_y$, which, for a small resistivity, implies a large current density. In fact, Figure 11 demonstrates the magnitude of resistivity required to reproduce the dissipation of the kinetic model. The graphs describe the time evolution of the y components of current density, and of the ratio of electric field and current density, at the major X point of the kinetic simulation. The latter graph corresponds to an equivalent resistivity. Partially owing to the reduced current density at the X point of the kinetic model, the equivalent resistivity appears to be very large, corresponding to magnetic Lundquist numbers of L = 1–10. Naturally, such effects are very difficult to reproduce in a resistive fluid model. We also stress that while a resistivity of the above magnitude is required to produce an electric field of the right magnitude if the current density is the same as in the kinetic model, a simple resistivity cannot reproduce the kinetic results. This fact is also borne out by the comparison above. Therefore a fluid model can only reproduce part of the kinetic evolution, and further work is required to decide whether this is sufficient for an adequate dissipation model within a larger-scale simulation.

The enhancement of the current density adjacent to the X point in the kinetic model, on the other hand, is related to details of the particle orbits, a feature that also cannot be reproduced in Hall-MHD. Similarly large differences, even ignoring the magnetic island structure, are found in the B_z magnetic field component normal to the current sheet, as evidenced by the middle panel of Figure 10. Here the graphs are,

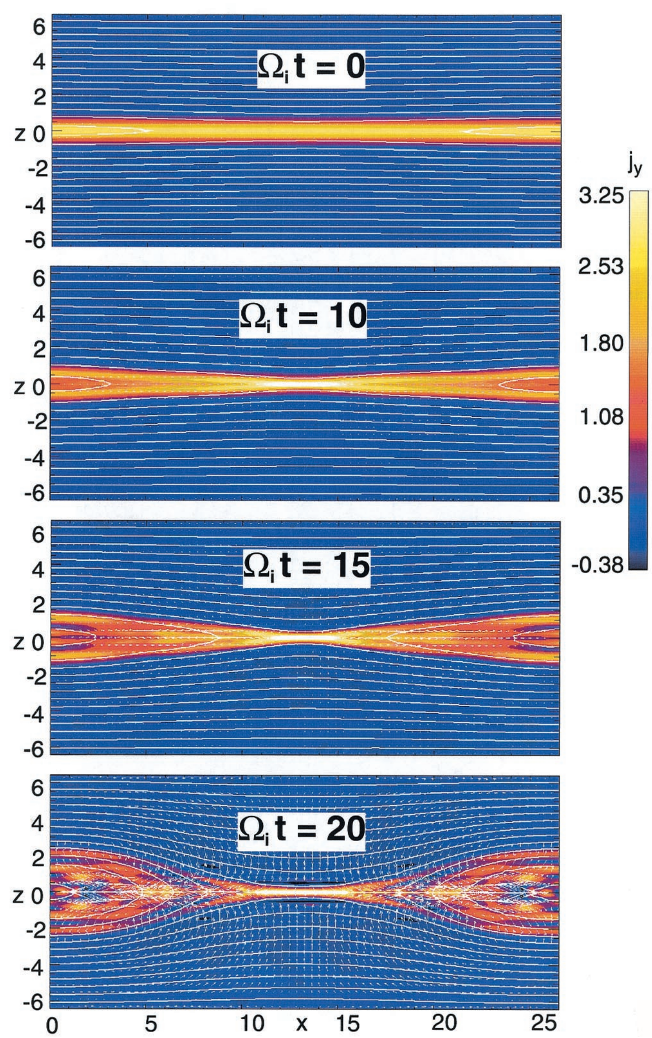

Plate 6. Magnetic field evolution and current density (color-coded) evolution for the Hall-MHD simulation. Ion flow vectors are shown also. The evolution appears to look similar to the kinetic model of Plate 1.

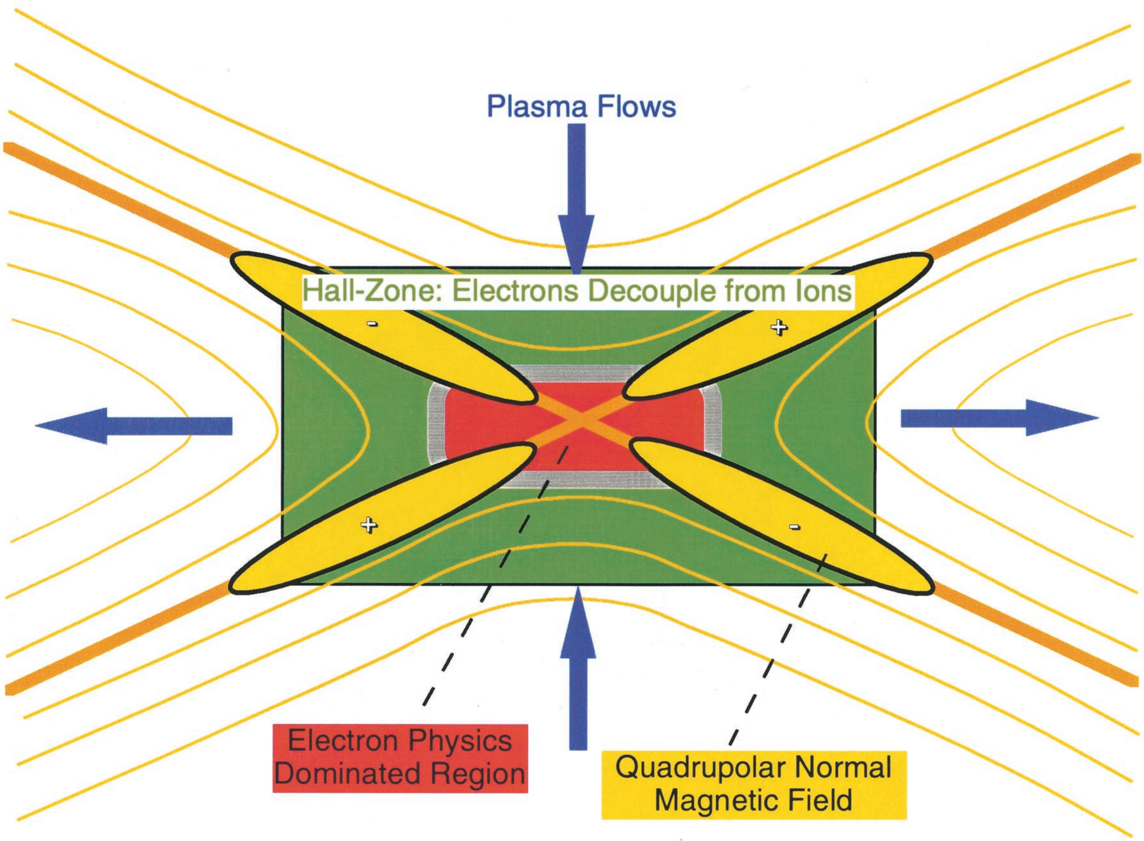

Plate 7. Neighborhood of the dissipation region in collisionless magnetic reconnection. The sketch shows the quadrupolar out-of-plane magnetic field; the Hall zone, where ions become unmagnetized; and the embedded, electron-physics-dominated electron diffusion region.

at best, similar, but a quantitative comparison at any location in x reveals differences of up to 100%. The integrals, however, are very similar, indicating similar amounts of reconnected magnetic flux. An explanation of the reason for this similarity is provided by the bottom panel of Figure 10, which features the convection electric field $E_c = v_{ex}B_z$ for both cases. Here it is noteworthy that amplitudes are actually very similar, in particular, if the presence of the island in the kinetic model is ignored. This similarity indicates that the transport of normal magnetic flux is similar for both models, giving rise to the similar evolutions of the reconnected magnetic flux.

Thus we find that the similarity of the Hall-MHD and kinetic models is superficial when the evolutions are compared in detail. In the interpretation of this result, however, it should be kept in mind that the system under study is still rather small, particularly if compared to typical ion parameters. On larger scales, evolutions are MHD-like and smaller-scale effects might play less of a role, as long as they foster similar electric fields and reconnection rates. It is therefore conceivable that the difference between Hall-MHD and kinetic models might become less and less important for increasing system size.

7. Summary and Conclusions

In this paper we presented an in-depth analysis of a fully electromagnetic, particle-in-cell simulation of magnetic reconnection. The simulation parameters were chosen to match those of the "reconnection challenge," defined by a modeling working group within the Geospace Environment Modeling (GEM) program of the National Science Foundation. The goal of this program was to compare simulations of the same reconnection configurations with the goal of understanding the physics underlying the reconnection process, as well as deriving ways to represent microphysical processes in macroscopic plasma models.

The results presented in this paper were primarily derived from the application of our particle-in-cell, fully electromagnetic simulation code, which has been applied to the reconnection problem in the past [e.g., *Hesse and Winske*, 1998; *Hesse et al.*, 1999]. The version applied to the present problem includes an implicit solver for the electromagnetic fields, which removes the Courant condition on light wave propagation.

During the evolution of the system in the simulation, the initial X point configuration led to the onset of fast magnetic reconnection after a period of adjustment. Similar to earlier calculations, a magnetic island formed by bifurcation of the initial reconnection site but became dissipated later in the evolution. An analysis of the current density contributions at the main X point proved that the electrons form a thin current sheet, of width comparable or slightly larger than the electron skin depth, and contribute most of the current flow in that region. Current density peaks were found adjacent to the central dissipation region, supported by electrons turned around by the increasing normal magnetic field.

The much faster electron and ion outflow from the recon-

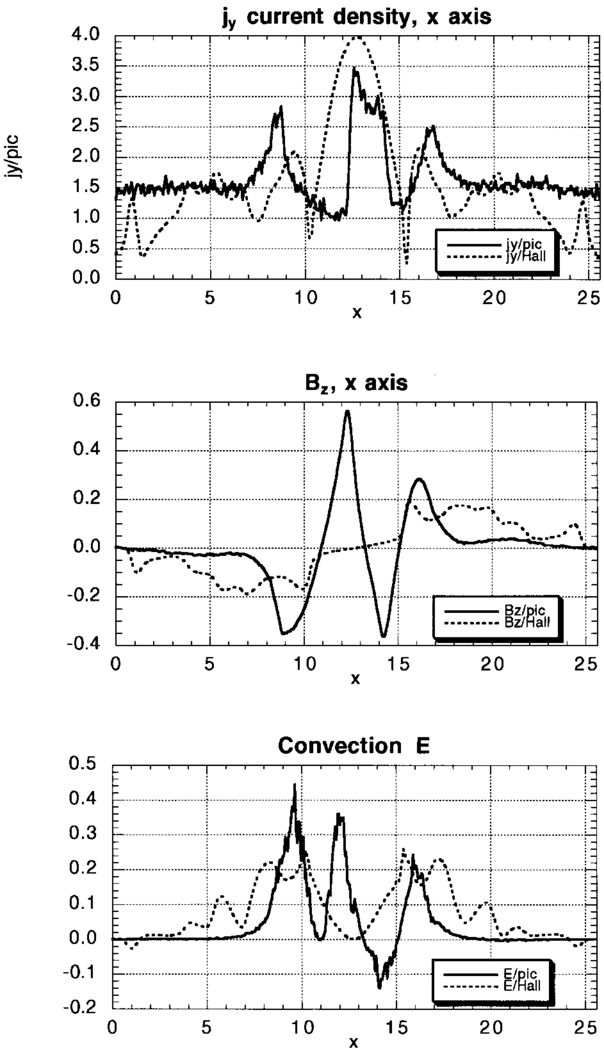

Figure 10. Comparison along the x axis between (top) current densities in the y (j_y) direction, (middle) magnetic normal components B_z, and (bottom) convection electric fields. Comparisons are for the particle simulation (solid lines) and Hall-MHD simulations (dotted lines), all for $\Omega_i t = 15$. While current densities and magnetic fields show very different distributions, the convection electric fields are considerably more similar.

nection region was related to the formation of a strong quadrupolar out-of-plane (B_y) magnetic field component, similar to what was found earlier in hybrid simulations [*Hesse and Winske*, 1994; *Drake and Mandt*, 1994]. An analysis of the amplitude of the B_y enhancement revealed some correlation with the rate of magnetic reconnection. The lack of a perfect correlation indicates that not just the amplitude but the gradient-scale length of B_y varies as well to determine the overall rate of reconnection. Contrary to this result, the peak electron and ion flow velocities correlate much better with reconnection rate, exhibiting higher flow velocities for higher reconnection electric fields.

Thus our studies support a reconnection region structure as sketched in Plate 7. The large-scale, MHD-like behavior transitions into a region, the so-called Hall zone, where ions become demagnetized, whereas electrons are still frozen to the magnetic field. This region is associated with the formation of a quadrupolar structure of the normal magnetic field, with gradients supporting current flow in the plane of the X-type magnetic field structure. The scale size of the Hall zone is a few to 10 ion inertial lengths, corresponding to one to a few thousand kilometers in the magnetotail of the Earth. Embedded in this latter region lies the electron dissipation region, where electrons become demagnetized from the magnetic field, thus enabling the reconnection process. The edges of this region are marked by peaks in nongyrotropic electron pressure. Scale sizes here are defined by the electron bounce motion in the reversals of both B_x and B_z, which typically correspond to just over an electron inertial length in the z direction and a few electron inertial lengths in the x direction. In the magnetotail these dimensions correspond to lengths of tens to hundreds of kilometers.

Since previous results had shown that the electric field in the diffusion region proper is provided by gradients of a nongyrotropic electron pressure tensor, we took the analysis further to the study of the actual electron and ion distribution functions in the diffusion region and right next to it. Here we found clear deviations from simple gyrotropy in both regions and for both species. Naturally, the electron distributions were most affected by the normal magnetic field in the vicinity of the X point in that higher-energy electrons experienced a strong acceleration in the x direction. At the X point proper a hot tail extending primarily in the u_y direction has been added to the bulk of the distribution, owing to acceleration in the reconnection electric field. Adjacent to this central region, the effects of the normal magnetic field bend this tail out of the u_y direction into a tilted configuration which includes the u_x direction also. This distorted distribution function gives rise to the occurrence of nongyrotropic, i.e., off-diagonal, components of the electron pressure tensor.

At this point a reader might wonder about the relation between our emphasis on electron anisotropy and the Whistler dynamics, emphasized by *Shay et al.* [this issue] and also found in our models (see, e.g., Plate 2). Whistler dynamics becomes important on scales comparable to the ion inertial length, whereas electron anisotropy requires electron bounce scales [*Hesse et al.*, 1999]. Therefore both processes operate on different scales, and both are necessary to facilitate magnetic reconnection. The reconnection rate is given by the electric field at the X point, which is dominated by derivatives of the electron pressure tensor in collisionless models, or by resistive effects in Hall-MHD models. Thus fast reconnection provided

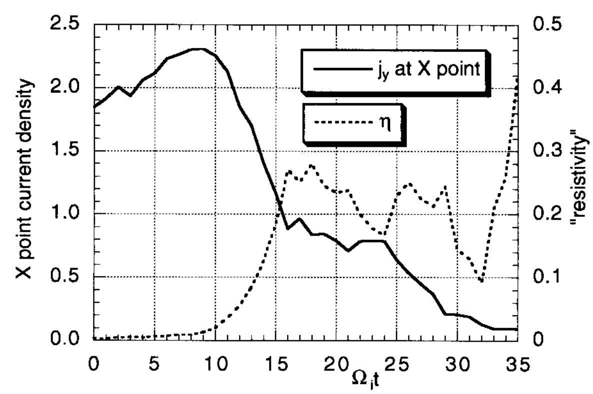

Figure 11. Current density and ratio of electric field and current density at the major X point of the particle simulation. The plot shows that very high resistivity values would be required to reproduce the structure of the kinetic dissipation region.

by Whistler dynamics is impossible unless a suitable dissipation is present. Our argument here is that in collisionless systems this dissipation is provided by electron pressure anisotropy.

As one might expect when considering the larger mass, the ions are much less affected by the normal magnetic field. Therefore the ion distributions at the X point proper and right next to it are very similar. Both exhibit a core around zero velocity in phase space, with a tail made of accelerated ions in the y direction of velocity space. The typical velocity of this tail, however, appeared to be much lower than in the case of the electrons, reflecting both the larger ion mass, which yields lower velocities when subjected to the same electric field, and the lower ion contribution to the current density. A detailed comparison between ion distributions taken at the two locations revealed a small influence of the normal magnetic field component, visible mostly in the ions with highest velocity in the y direction.

We then left the detailed study of an individual simulation in order to perform investigations of the impact of sheet thickness and electron mass. For this purpose we performed two additional simulations, starting from configurations which differed from the above, "standard" run only by the width of the initial current sheet. The first, "narrow" sheet run utilized half the sheet width of the standard simulation, whereas the second, "wide" configuration featured twice the initial sheet width. As might be expected, the evolutions of all three runs differed greatly. The fastest, narrow run exhibited multiple bifurcations of the reconnection site and formation of magnetic islands during the fastest of all three evolutions. The wide run, on the other hand, evolved the slowest, with the simplest configuration, consisting of a single X point during the entire development.

From a very simple linear analysis of the acceleration of the plasma sheet plasma by the initial perturbation, we found the evolution timescale to be proportional to the current sheet width. We tested this estimate in two ways. First, we compared the peak value of the reconnection electric field in all three cases to the inverse of the current sheet thickness. Here we found an almost perfect linear relation with the inverse of the current sheet thickness, consistent with our simple analysis. Second, we investigated the relationship between the sheet thickness and the time to reach a set perturbation level, defined by the amount of magnetic flux normal to the current sheet. This evolution time showed deviations from the linear dependence, indicating the limitations of our simple analysis. Nevertheless, the deviations were found to be small, so that within the range of parameters considered the characteristic evolution time can be considered as approximately linearly dependent on the current sheet width.

The last step of the studies presented in the present paper dealt with a comparison of Hall-MHD simulations of the same system with the kinetic model. This comparison was motivated by the fact that other kinetic simulations of the same system featured the virtually same large-scale evolution, with larger differences restricted to the electron dynamics near the reconnection site [*Hesse et al.*, 1999]. This observation supported the conclusion that the nature of the dissipation process might be less important, leading to similar large-scale behavior irrespective of dissipation details. This supposition is also borne out by hybrid simulations published in an accompanying paper [*Kuznetsova et al.*, this issue], which generate an almost identical large-scale evolution based on a simpler fluid electron model.

Images of the overall evolution and, in particular, the growth of the reconnected magnetic flux behaved almost identically for Hall-MHD and the kinetic model. A more detailed comparison of the simulations, however, revealed substantial differences in the flow velocities, which were consistently higher in the Hall-MHD case, and the distribution of the normal magnetic field. Interestingly, and reflecting the match of the reconnected magnetic flux, the values of the convection electric field, defined by the product of electron flow velocity and magnetic field, yielded rather similar results. On the basis of this study we concluded that a detailed match between simple fluid models and a fully kinetic model might be different to achieve. In part, this may be true because of the size of the system, which extends for only a few tens of typical ion Larmor radii. Thus the small system size may emphasize deviations from simple isotropy in the ions as well, which are not represented in a fluid model such as Hall-MHD. On larger scales, however, the most important quantity communicated between small and large scales should be the electric field, and this appears to be reasonably well described even in our Hall-MHD model. Therefore our results clearly show that Hall-MHD is inadequate to represent the kinetic model on small scales, but our results leave open the option that it might constitute a sufficiently good representation of the dissipation on larger scales.

Acknowledgments. This work was supported by NASA's Sun-Earth-Connection Theory and Supporting Research and Technology Programs.

Janet G. Luhmann thanks Amitava Bhattacharjee and another referee for their assistance in evaluating this paper.

References

Antiochos, S. K., C. R. DeVore, and J. A. Klimchuk, A model for solar coronal mass ejections, *Astrophys. J.*, in press, 2001.

Atkinson, G., Field-line merging and slippage, *Geophys. Res. Lett.*, *5*, 465, 1978.

Birn, J., and M. Hesse, Geospace Environment Modeling (GEM) magnetic reconnection challenge: Resistive tearing, anisotropic pressure, and Hall effects, *J. Geophys. Res.*, this issue.

Birn, J., et al., Global Environment Modeling (GEM) magnetic reconnection challenge, *J. Geophys. Res.*, this issue.

Brueckner, G. E., Global coronal disturbances as the source for the low latitude solar wind, *Eos Trans. AGU*, *77*(46), Fall Meet. Suppl., F561, 1996.

Cai, H. J., and L. C. Lee, The generalized Ohm's law in collisionless magnetic reconnection, *Phys. Plasmas*, *4*, 509, 1997.

Cargill, P. A., and J. A. Klimchuk, A nanoflare explanation for the heating of coronal loops observed by Yohkoh, *Astrophys. J.*, *478*, 799, 1997.

Drake, J. F., and M. E. Mandt, Structure of thin current layers: Implications for magnetic reconnection, *Phys. Rev. Lett.*, *73*, 1251, 1994.

Gosling, J. T., J. Birn, and M. Hesse, Three-dimensional magnetic reconnection and the magnetic topology of coronal mass ejection events, *Geophys. Res. Lett.*, *22*, 869, 1995.

Haerendel, G., On the potential role of field-aligned currents in solar physics, paper presented at 21st ESLAB Symposium, Bolkesjø, Norway, Eur. Space Agency, Paris, 1987.

Hesse, M., and D. Winske, Hybrid simulations of collisionless ion tearing, *Geophys. Res. Lett.*, *20*, 1207, 1993.

Hesse, M., and D. Winske, Hybrid simulations of collisionless reconnection in current sheets, *J. Geophys. Res.*, *99*, 11,177, 1994.

Hesse, M., and D. Winske, Electron dissipation in collisionless magnetic reconnection, *J. Geophys. Res.*, *103*, 26,479, 1998.

Hesse, M., D. Winske, J. Birn, and M. Kuznetsova, Predictions and explanations of plasma sheet dissipation processes: Current sheet kinking, in *Substorms-4*, p. 437, Terra Sci., Tokyo, 1998.

Hesse, M., K. Schindler, J. Birn, and M. Kuznetsova, The diffusion region in collisionless magnetic reconnection, *Phys. Plasmas*, *6*, 1781, 1999.

Hewett, D. W., G. E. Frances, and C. E. Max, New regimes of magnetic reconnection in collisionless plasma, *Phys. Rev. Lett*., *61*, 893, 1988.

Horiuchi, R., and T. Sato, Particle simulation study of driven magnetic reconnection in a collisionless plasma, *Phys. Plasmas*, *1*, 3587, 1994.

Horiuchi, R., and T. Sato, Particle simulation study of collisionless driven reconnection in a sheared magnetic field, *Phys. Plasmas*, *4*, 277, 1997.

Krauss-Varban, D., and N. Omidi, Large-scale hybrid simulations of the magnetotail during reconnection, *Geophys. Res. Lett*., *22*, 3271, 1995.

Kuznetsova, M., M. Hesse, and D. Winske, Kinetic quasi-viscous and bulk flow inertia effects in collisionless magnetotail reconnection, *J. Geophys. Res*., *103*, 199, 1998.

Kuznetsova, M., M. Hesse, and D. Winske, Collisionless reconnection supported by nongyrotropic pressure effects in hybrid and particle simulations, *J. Geophys. Res*., this issue.

Langdon, A. B., On enforcing Gauss' law in electromagnetic particle-in-cell codes, *Comput. Phys. Commun*., *70*, 447, 1992.

Lin, Y., and D. W. Swift, A two-dimensional hybrid simulation of the magnetotail reconnection layer, *J. Geophys. Res*., *101*, 19,859, 1996.

Lottermoser, R.-F., M. Scholer, and A. P. Matthews, Ion kinetic effects in magnetic reconnection: Hybrid simulations, *J. Geophys. Res*., *103*, 4547, 1998.

Ma, Z. W., and A. Bhattacharjee, Fast impulsive reconnection and current sheet intensification due to electron pressure gradients in semi-collisional plasmas, *Geophys. Res. Lett*., *23*, 1673, 1996.

Nagai, T., et al., Structure and dynamics of magnetic reconnection for substorm onsets with Geotail observations, *J. Geophys. Res*., *103*, 4419, 1998.

Otto, A., Geospace Environment Modeling (GEM) magnetic reconnection challenge: MHD and Hall MHD–constant and current dependent resistivity models, *J. Geophys. Res*., this issue.

Paschmann, G., B. U. Ö. Sonnerup, I. Papamastorakis, N. Sckopke, G. Haerendel, S. J. Bame, J. R. Asbridge, J. T. Gosling, C. T. Russell, and R. C. Elphic, Plasma acceleration at the Earth's magnetopause: Evidence for reconnection, *Nature*, *282*, 243, 1979.

Priest, E. R., Magnetic reconnection at the Sun, in *Magnetic Reconnection in Space and Laboratory Plasmas*, *Geophys. Monogr. Ser*., vol. 30, edited by E. W. Hones, p. 63, AGU, Washington, D. C., 1984.

Pritchett, P. L., Effect of electron dynamics on collisionless reconnection in two-dimensional magnetotail equilibria, *J. Geophys. Res*., *99*, 5935, 1994.

Pritchett, P. L., Geospace Environment Modeling (GEM) magnetic reconnection challenge: Simulations with a full particle electromagnetic code, *J. Geophys. Res*., this issue.

Shay, M. A., and J. F. Drake, The role of electron dissipation on the rate of collisionless magnetic reconnection, *Geophys. Res. Lett*., *25*, 3759, 1998.

Shay, M. A., J. F. Drake, R. E. Denton, and D. Biskamp, Structure of the dissipation region during collisionless magnetic reconnection, *J. Geophys. Res*., *103*, 9165, 1998.

Shay, M. A., J. F. Drake, B. N. Rogers, and R. E. Denton, Alfvenic collisionless magnetic reconnection and the Hall term, *J. Geophys. Res*., this issue.

Sonnerup, B. U. Ö., et al., Evidence for magnetic field reconnection at the Earth's magnetopause, *J. Geophys. Res*., *86*, 10,049, 1981.

Tanaka, M., Macro-particle simulations of collisionless magnetic reconnection, *Phys. Plasmas*, *2*, 2920, 1995a.

Tanaka, M., The macro-em particle simulation method and a study of collisionless magnetic reconnection, *Comput. Phys. Commun*., *87*, 117, 1995b.

Vasyliunas, V. M., Theoretical models of magnetic field line merging, 1, *Rev. Geophys*., *13*, 303, 1975.

Villasenor, J., and O. Buneman, Rigorous charge conservation for local electromagnetic field solvers, *Comput. Phys. Commun*., *69*, 306, 1992.

J. Birn, Los Alamos National Laboratory, Los Alamos, NM 87545.

M. Hesse, Electrodynamics Branch, NASA Goddard Space Flight Center, Code 696, Greenbelt, MD 20771. (michael.hesse@gsfc.nasa.gov)

M. Kuznetsova, Raytheon STX, NASA Goddard Space Flight Center, Greenbelt, MD 20771.

(Received August 4, 1999; revised March 8, 2000;
accepted April 4, 2000.)